

pubs.acs.org/macroletters Letter

Shear-Modulated Rates of Phase Transitions in Sphere-Forming Diblock Oligomer Lyotropic Liquid Crystals

Connor S. Valentine, Ashish Jayaraman, Mahesh K. Mahanthappa,* and Lynn M. Walker*



Cite This: ACS Macro Lett. 2021, 10, 538-544



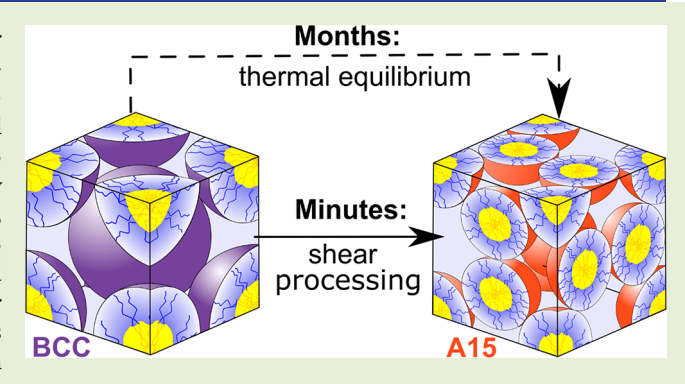
ACCESS

Metrics & More

Article Recommendations

S Supporting Information

ABSTRACT: Hydration of the amphiphilic diblock oligomer $C_{16}H_{33}(CH_2CH_2O)_{20}OH$ ($C_{16}E_{20}$) leads to concentration-dependent formation of micellar body-centered cubic (BCC) and Frank–Kasper A15 lyotropic liquid crystals (LLCs). Quiescent thermal annealing of aqueous LLCs comprising 56–59 wt % $C_{16}E_{20}$ at 25 °C after quenching from high temperatures established their ability to form short-lived BCC phases, which transform into long-lived, transient Frank–Kasper σ phases en route to equilibrium A15 morphologies on a time scale of months. Here, the frequency and magnitude of applied oscillatory shear show the potential to either dynamically stabilize the metastable BCC phase at low frequencies or increase the rate of formation of the A15 to minutes at high frequencies. Time-resolved synchrotron small-angle X-ray scatter-



ing (TR-SAXS) provides in situ characterization of the structures during shear and thermal processing. This work shows that the LLC morphology and order—order phase transformation rates can be controlled by tuning the shear strain amplitude and frequency.

mphiphiles self-assemble in selective solvents to yield A temperature- and concentration-dependent lyotropic liquid crystal (LLC) morphologies, including 1D lamellae, bicontinuous networks, hexagonally packed cylindrical micelles (H_I), and ordered 3D packings of spherical micelles. 1-3 Typical micellar arrangements include high-symmetry bodycentered cubic (BCC), face-centered cubic (FCC), and hexagonally closest-packed (HCP) phases.^{4–8} Recent studies of aqueous LLCs of small amphiphiles have also revealed their ability to form lower symmetry packings known as Frank–Kasper (FK) phases. 9–12 Such complex micellar packings have also been observed in solventless thermotropic liquid crystals^{13–15} and block polymer soft materials. ^{16–20} FK phases are characterized by large unit cells comprising ≥7 micelles of at least two different volumes. 21,22 For example, the FK A15 phase consists of two populations of quasi-spherical micelles where the aggregation number varies by ±3% around a mean value.²³ Phase transitions among these complex structures have been induced by controlling thermal processing history under quiescent conditions, some of which mimic metallurgical processing procedures. 19,20,23

Unlike metallic crystals, LLC phases of packed micelles can be easily manipulated at the micelle, lattice, and grain size length scales by using relatively weak external forces. In these soft systems, shear is effective in enabling long-range structure and grain orientation refinement resulting in pseudomonodomain crystals of soft materials. Shearing of ordered micellar phases results in micelle deformation, reorientation, and slipping along lattice planes to relieve stress

accumulation in the structure. $^{33-35}$ Reports of the use of shear high shear rates ($\dot{\gamma} > 100~\rm s^{-1}$) to drive "shear-induced melting" of ordered phases into disordered micellar fluids and modify order-to-order transitions (OOTs) of micellar materials have largely been limited to canonical BCC, FCC, and $\rm H_{I}$ phases. 25,28,36,37 Time-varying or oscillatory shear fields applied while cooling an aqueous lyotropic FCC phase of a poly(isoprene-*block*-ethylene oxide) diblock polymer enabled observation of transitions into structures exhibiting 12-fold and 18-fold rotational symmetries. 38 There are no reports of using shear to alter the rate of formation of a specific crystal phase. Herein, we show that the formation of the FK A15 phase can be sped up or entirely suppressed by tuning the frequency and strength of a simple oscillatory shear field.

Jayaraman et al. showed previously unrecognized aqueous LLC self-assembly behaviors of the nonionic diblock oligomer $C_{16}H_{33}(CH_2CH_2O)_{20}OH$ ($C_{16}E_{20}$ or Brij 58). With decreasing hydration, quiescent X-ray scattering analysis revealed that $C_{16}E_{20}$ exhibits the concentration-dependent phase sequence FCC \rightarrow BCC \rightarrow A15 \rightarrow H_I at 25 °C. Different underlying micellar arrangements in these phases lead to subtle differences

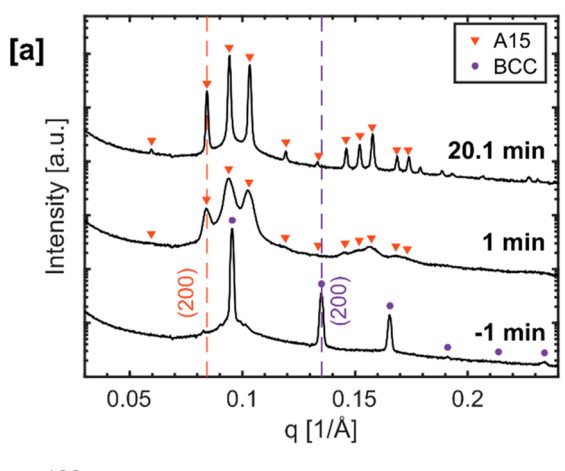
Received: March 8, 2021 Accepted: April 16, 2021



in their viscoelastic rheological signatures under oscillatory shear, as recently established for the FCC and BCC morphologies.³⁹ Quiescent heating of the A15 phase formed between 56 and 59 wt % C₁₆E₂₀ in H₂O triggers an OOT into a BCC phase at 57 °C, which transforms into a H_I phase at 70 °C. Subsequent quenching of the H_I phase to 25 °C results in an initial OOT to a nonequilibrium BCC phase that exhibits a broad SAXS signature that is different from that of the hightemperature BCC phase. Subsequent isothermal annealing of this quenched sample at 25 °C leads to the nucleation and growth of a FK σ phase within 1 h. Extended annealing of the well-developed σ phase at 25 °C results in slow nucleation of the equilibrium A15 phase after several days with complete transformation after 5 months. The slow BCC $\rightarrow \sigma \rightarrow A15$ transition in this system provides an opportunity to quantify the impact of shear processing, specifically, the frequency and strength of an oscillatory shear field on OOT kinetics.

In this work, we apply a well-defined oscillatory shear, $\gamma(f,t)$ = $\gamma_0 \sin(2\pi ft)$, as a canonical shear deformation. Use of an oscillatory deformation facilitates control of both the frequency, f, and the strength, γ_0 , of the deformation while limiting the chances of tearing or gross failure of the sample. We use this well-defined deformation to modulate the kinetics of the isothermal BCC $\rightarrow \sigma \rightarrow$ A15 transition at 25 °C in aqueous C₁₆E₂₀ samples in the narrow 57–59 wt % amphiphile composition range. Time-resolved synchrotron small-angle Xray scattering (TR-SAXS) is used to collect structural information every 5 s with an X-ray exposure time of 0.1 s while oscillatory shear is applied by using a parallel-plate shear cell. The strains applied are sufficiently greater than the linear plateau in moduli observed during strain amplitude sweeps per our previous work with $C_{16}E_{20}$. While oscillatory shear flow is a central pillar of rheometric studies, we do not use the deformation to extract mechanical behavior or material properties; the linearity or nonlinearity of the constitutive behavior is not a focus of this work. Shear is applied only as a well-controlled deformation. All samples are initially heated to 70 °C for 1 min to induce H_I phase formation and subsequently cooled to 25 °C at a rate of 30 °C/min. Immediately upon cooling to 25 °C a BCC phase is observed. After equilibration at 25 °C for 5 min, oscillatory shear is initiated.

Figure 1 shows the impact of shear at a frequency f = 1.0 Hzand strain amplitude $\gamma = 1770\%$ on the BCC to A15 phase transition at 25 °C. Before shear is initiated (t < 0 min), the sample forms a BCC phase with unit cell parameter $a_{\rm BCC} = 9.3$ nm as evidenced by the SAXS maxima at $(q/q^*)^2 = 1, 2, 3, ...$ (Figure 1a, purple circles). The quiescent thermal equilibration continues at 25 °C until t = 0 min, when oscillatory shear is initiated. After 1 min of shear (t > 1 min), the BCC reflections are entirely absent from the SAXS data, and they are replaced with the somewhat broad (110), (200), (210), and (211) reflections of the A15 phase (Figure 1a). Red triangles denote the calculated positions of the first 11 A15 peaks with unit cell parameter $a_{A15} = 14.9$ nm. Continued application of shear results in intensified and narrowed SAXS peaks, which indicates grain size coarsening.⁴⁰ The isothermal BCC-to-A15 transition is monitored under shear by tracking the intensity of the (200) SAXS peak for each of the two phases. The (200) peaks were selected due to minimal overlap with other peaks and their equal reflection multiplicities. Standard peak fitting algorithms were used to extract peak locations and



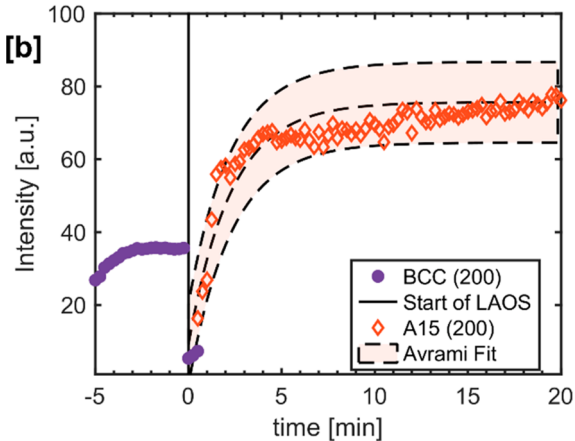


Figure 1. (a) 1D-SAXS profiles at time points before and during oscillatory shear $(f=1.0 \text{ Hz}, \gamma=1770\%)$, initiated at t=0 min. Calculated peak positions for BCC with unit cell parameter $a_{\rm BCC}=9.3$ nm (purple circles) and A15 with lattice parameter $a_{\rm A15}=14.9$ nm (red triangles) are overlaid. (b) Time evolution of $I_{200}({\rm BCC})$ and $I_{200}({\rm A15})$ before and during shear. $I_{200}({\rm A15})$ data are fit to the Mehl–Johnson–Avrami (MJA) equation and shown with shaded 95% confidence intervals. Every third data point is shown for clarity; see the Supporting Information for complete profiles.

intensities in MATLAB (see the Supporting Information for analysis details).

The time evolution of I_{200} is shown for each phase in Figure 1b. Mehl–Johnson–Avrami (MJA) nucleation theory $^{41-44}$ offers a natural framework for quantifying the kinetics of the isothermal oscillatory shear modulated BCC \rightarrow A15 OOTs across a range of shear conditions. We specifically modeled the time evolution of the peak intensity $I_{200}({\rm A15})$ derived from TR-SAXS analyses using the simplified MJA model

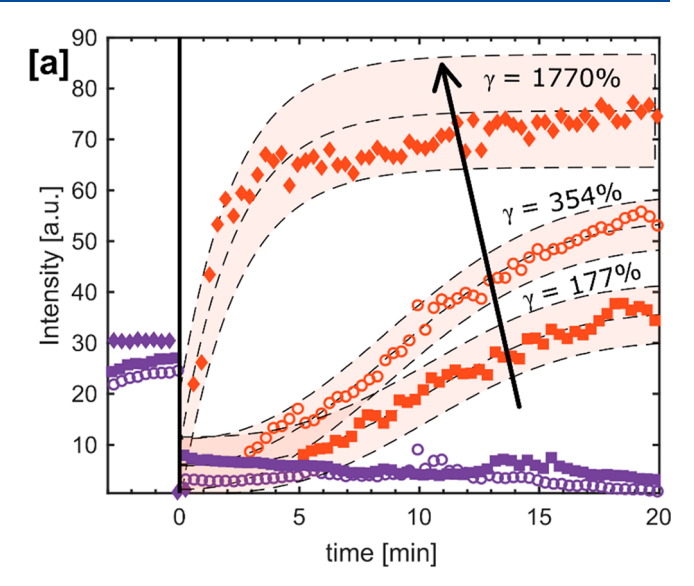
$$I(t) - I(t_0) = [I(t_\infty) - I(t_0)](1 - e^{-k(t-t_0)^n})$$

where $I(t_0)$ and $I(t_\infty)$ are the intensities of the A15 (200) peak at initiation (t=0 min) and upon cessation of shear (t=20 min). k is the phase transformation rate constant and from this model, and $\tau=k^{-(1/n)}$ is a characteristic phase transformation time scale. For the purposes of this Letter, we primarily seek to use this model to parametrize the kinetics of the isothermal BCC \rightarrow A15 transition under shear processing. The A15 phase formation is captured well by the MJA fit, shown with shaded 95% confidence intervals throughout the text and in the Supporting Information.

The rapid and direct, shear-induced transition from BCC \rightarrow A15 significantly differs from the slower, indirect BCC $\rightarrow \sigma \rightarrow$ A15 transition sequence observed during quiescent isothermal annealing.²³ In the latter report, signatures of the A15 phase emerge only after several days with the complete phase transformation after 150 days at 25 °C. We note that those quiescent phase behavior studies employed small samples enclosed in metal pans that were cooled by immersion into a thermostated water bath. To understand whether the cooling rate and geometry of the parallel-plate shear cell used in our TR-SAXS studies influenced the OOT pathways and kinetics, we performed a control experiment where no shear is applied at t = 0 min after the thermal annealing procedure outlined above (Figure S1). TR-SAXS analyses of this quiescent sample reveal somewhat slower σ phase nucleation kinetics, which we ascribe to slight differences in sample cooling rate and composition. Despite these small differences, our control experiment provides baseline kinetics to establish that oscillatory shear suppresses σ phase formation and triggers an accelerated BCC → A15 OOT within minutes rather than months in comparison to quiescent thermal annealing.

To explore the impact of shear processing, we demonstrate the effect of strain amplitude, γ_0 , on the BCC $\rightarrow \sigma \rightarrow A15$ transition under shear of the same frequency, f = 1.0 Hz (Figure 2a). The time evolution of I_{200} is shown for each phase, with the resulting MJA fit shown for $I_{200}(A15)$ in Figure 2a. As the strain amplitude is decreased by an order of magnitude from 1770% to 177%, the rate of A15 formation slows (see Figures S2-S4 for full time-resolved profiles). Figure 2b shows the 1D-SAXS traces obtained at t = 20 min of oscillatory shear under these conditions. Results of the quiescent control experiment where no shear is applied for ~20 min (Figure S1) are included for comparison. The BCC peaks for the control experiment appear at slightly lower q values as the sample was at the lower end of the concentration window (57–59 wt %), corresponding to an incremental change in $a_{BCC} = 9.3$ to a_{BCC} = 9.5 nm. An increase in the BCC unit cell size with decreasing C₁₆E₂₀ concentration has been previously reported in this system.²³ Peaks that are not labeled with markers for the calculated A15 or BCC peak positions correspond to the σ phase, which is the expected intermediate structure.²³ Increasing γ_0 at this frequency increases the rate of A15 formation, decreases the intensity of residual σ and BCC reflections, and leads to larger grain sizes after 20 min of shear as shown by qualitatively sharper SAXS peaks in Figure 2b. Similar trends are observed for shear experiments conducted at a higher frequency f = 9.9 Hz with $3.54\% \le \gamma_0 \le 177\%$ (Figures S5–S8).

Lowering the frequency of the deformation to 0.1 Hz drastically changes the dependence of the BCC \rightarrow A15 transition kinetics on applied strain amplitude in the range 177 $\leq \gamma_0 \leq$ 1770% (Figure 3 and Figures S9–S11). In contrast to the observations at 1.0 Hz (Figure 2) and 9.9 Hz (Figures S5–S8), increasing the strain amplitude decreases the rate of A15 formation. Remarkably, the highest strain amplitude oscillatory shear applied at 0.1 Hz suppresses the formation of both A15 and σ for the duration of the experiment. At the end of the 20 min oscillatory shear process, only two low-intensity SAXS maxima are visible near the expected q values for the (200) and (211) reflections (second and fourth SAXS peaks) of the A15 phase in Figure 3b. In this case, slow growth of the A15 phase prevents a reliable MJA fit. However, it is evident that the time scale of A15 formation under these conditions is significantly



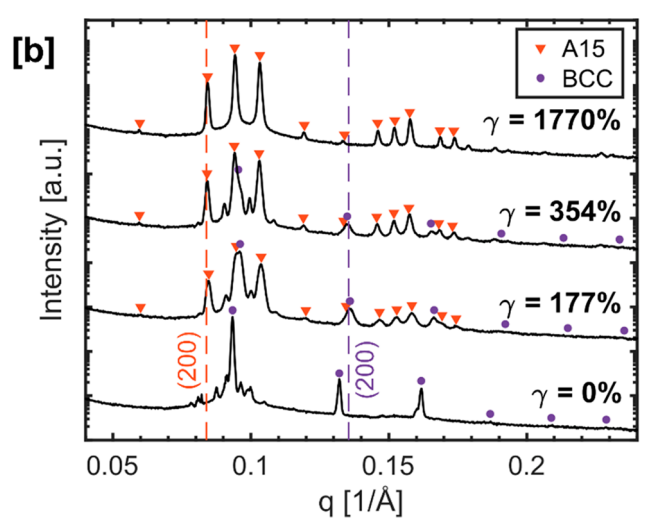


Figure 2. (a) Time evolution of $I_{200}(BCC)$ and $I_{200}(A15)$ for three separate shear trials, demonstrating the effect of strain amplitude at f=1.0 Hz. Oscillatory shear is initiated at t=0 min. BCC data (purple) and A15 data (red) share the same symbol shape at each strain amplitude. $I_{200}(A15)$ data are fit the Mehl–Johnson–Avrami (MJA) equation and shown with shaded 95% confidence intervals. Every fourth data point is shown for clarity; see Figures S2–S4 for complete profiles. (b) 1D-SAXS profiles at t=20 min of oscillatory shear compared to the control case where no shear is applied for ~20 min. Calculated peak positions for BCC (purple circles) and A15 (red triangles) are overlaid.

longer than the other oscillatory shear conditions tested (τ > 100 min).

The time scale for A15 formation (τ) which results from the MJA fits to each oscillatory shear experiment is shown in Figure 4 (see Figure S12 for associated model fits of k and n). Error bars are shown and are typically smaller than the size of the markers. For both f=1.0 and 9.9 Hz (filled symbols) τ monotonically decreases with increasing strain amplitude, indicating an acceleration of the BCC-to-A15 transition. A different trend holds at f=0.1 Hz (open purple symbols). At this low frequency, increasing strain amplitude slows the kinetics of the BCC \rightarrow A15 transition such that the slow growth kinetics at $\gamma_0=1770\%$ prevent reliable extraction of MJA fit parameters. Under these low-frequency and high-

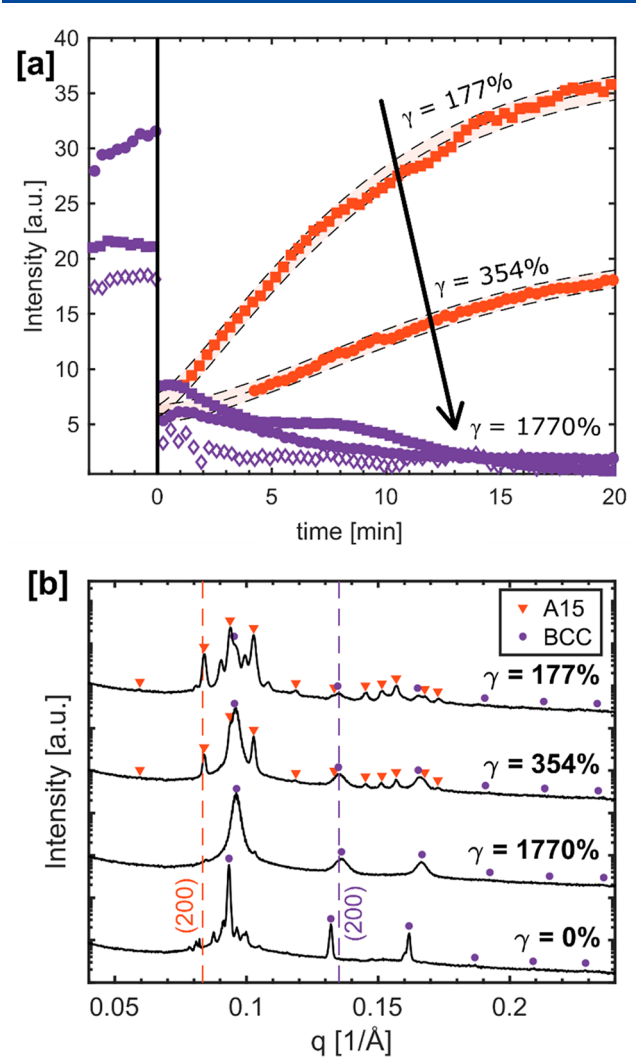


Figure 3. (a) Time evolution of $I_{200}(BCC)$ and $I_{200}(A15)$ for three separate shear trials, demonstrating the effect of strain amplitude at f=0.1 Hz. Oscillatory shear is initiated at t=0 min. BCC data (purple) and A15 data (red) share the same symbol shape at each strain amplitude. $I_{200}(A15)$ data are fit the Mehl–Johnson–Avrami (MJA) equation and shown with shaded 95% confidence intervals. Every fourth data point is shown for clarity; see the Supporting Information for complete profiles. (b) 1D-SAXS profiles at t=20 min of shear, compared to the control case where no shear is applied for ~ 20 min. Calculated peak positions for BCC (purple circles) and A15 (red triangles) are overlaid.

strain-amplitude conditions, τ is evidently much longer than every other shear condition tested (indicated by the purple arrow) and may even be longer than the quiescent case.

Finally, we use the maximum shear rate applied during oscillatory shear ($\dot{\gamma}=2\pi f\gamma_0$) to clarify trends in the time scale of A15 formation (τ) between low-, intermediate-, and high-frequency trials (Figure 4b). The maximum shear rate during oscillatory shear represents the rate at which deformations to the sample are applied at the peak of the sinusoidal oscillation cycle. By replotting the data in Figure 4a using this reduced form that incorporates both γ_0 and f, we find that increasing $\dot{\gamma}$ during oscillatory shear decreases τ for A15 formation only when the frequency of oscillation is sufficiently rapid (f=1.0 and 9.9 Hz, filled symbols). These data follow a simple power-law scaling with an exponent of -0.57 ± 0.18 , as indicated by the linear fit of the log-log plot, suggesting a scaling with rate

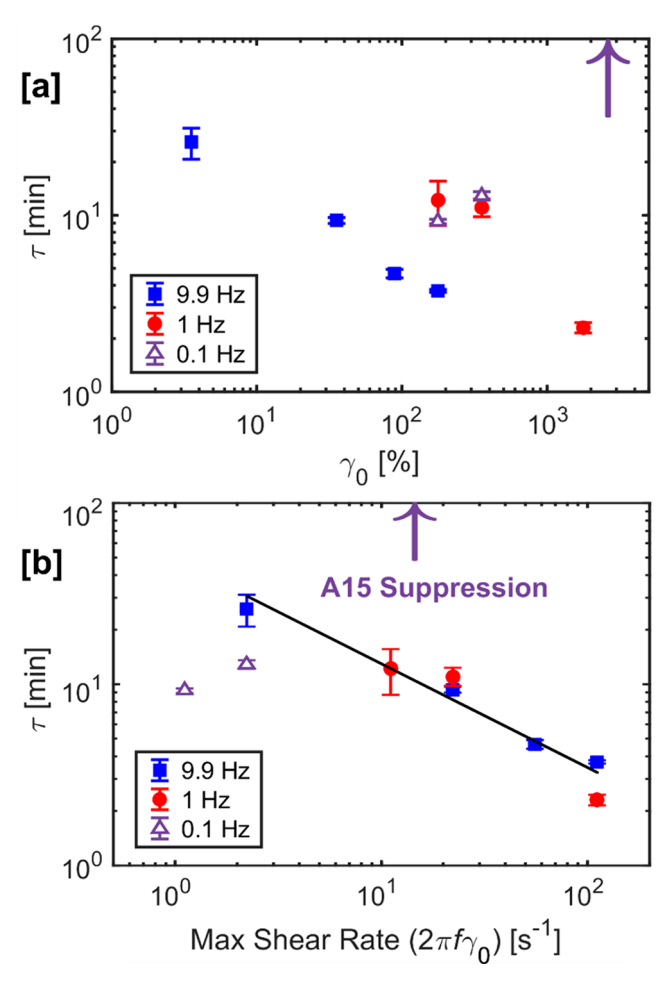


Figure 4. (a) Time scale for A15 formation (τ) from the MJA model versus applied γ_0 for each shear condition with f=9.9 Hz (filled blue squares), 1.0 Hz (filled red circles), and 0.1 Hz (open purple triangles). A purple arrow denotes that τ is dramatically longer than 100 min when $\gamma_0=1770\%$ and f=0.1 Hz. In most cases, the calculated error bars are smaller than the size of the markers. (b) Trends in τ with maximum shear rate during oscillatory shear deformation. The maximum shear rate during oscillatory shear is proportional to the frequency multiplied by the strain amplitude. A simple power-law scaling with an exponent of -0.57 ± 0.18 is fit to data of intermediate and high frequency (filled symbols).

or time scale or deformation rather than strain. However, the data collected at f=0.1 Hz (open purple symbols) do not follow this trend: instead, increasing the effective shear rate of a low frequency oscillation results in a drastic increase in τ . The purple arrow in Figure 4b again indicates the f=0.1 Hz and $\gamma_0=1770\%$ oscillatory shear condition that resulted in nearly complete A15 suppression.

The BCC $\rightarrow \sigma \rightarrow A15$ transition has been argued to stem from a combination of intermicellar chain exchange to achieve the prerequisite aggregation number distribution with minimal interfacial area for phase formation and micelle diffusion to appropriate symmetry-equivalent positions in the lattice. 9,21,45 For example, in 58.9 wt % C₁₆E₂₀ the average aggregation number (N_{AGG}) for the A15 phase is ~128.2, while for BCC, $N_{AGG} \sim 123.2$. The small difference in aggregation numbers is achieved through intermicellar chain exchange in the quiescent case. However, the results presented here suggest that macroscopic deformation during shear alters or even suppresses the nanoscale mechanisms that mediate these phase

transitions. If the BCC phase were replaced directly by the A15 phase via chain exchange and micelle diffusion, we expect an Avrami-style fit to capture the growth of the A15 phase as well as the reduction of the BCC phase as seen in quiescent thermal annealing studies. 41 Instead, we observe a large, almost instantaneous decrease in intensity of BCC peaks upon initiation of shear, followed by a slow increase in the magnitude of peaks corresponding to the A15 structure. Chain exchange and micelle diffusion alone cannot account for this observation. We speculate that the nonlinear strain applied during oscillatory shear immediately breaks the metastable BCC phase to possibly yield a poorly ordered micellar arrangement, which falls into the equilibrium A15 arrangement with minimal corona overlap. 46,47 Subsequent application of high-frequency shear facilitates intermicellar collisions and chain exchange³⁶ to equilibrate the micelle aggregation numbers to achieve minimal interfacial area, enabling nucleation and growth of a well-ordered, equilibrium A15 structure from the poorly ordered intermediate micellar phase.

Sufficiently high frequency shear-induced spatial displacement of the micelles coupled with accelerated chain exchange likely drives the approach to the equilibrium A15 phase from the metastable BCC phase. The cause of the decrease in rate and even suppression of A15 nucleation observed during low frequency oscillations is not clear. A possible explanation stems from the realization that low-frequency oscillatory flow approaches steady state, unidirectional flow, especially at these large amplitudes. For steady shear flow $(f \rightarrow 0)$, the mechanism could shift to one in which the crystalline planes slip and yield to alleviate accumulated stress in the structure. The high-symmetry BCC structure with 12 independent lattice slip systems does provide more efficient pathways for energy dissipation as compared to three independent slip systems that characterize the relatively less ductile A15 phase. 48,49 Hence, nucleation of complex FK structures is delayed under conditions approaching steady shear achieved only at the lowest frequency and highest strain applied in this work. The observed (albeit slow) formation of the A15 structure upon cessation of the shear under these last conditions corroborates this hypothesis.

In summary, we have demonstrated that shear processing of aqueous LLCs of C₁₆E₂₀ enables control over the kinetics of the metastable BCC → equilibrium A15 phase transition at 25 °C. Shear processing accelerates the phase transition from BCC → A15 by several orders of magnitude as compared to the quiescent case. At f = 1 and 9.9 Hz, increasing the shear rate increases the rate of A15 formation. In contrast, at the lowest applied frequency 0.1 Hz, increasing the shear rate slows the rate of A15 formation. Combining a low f with a high γ_0 entirely arrests the BCC structure, rendering the time scale for A15 formation immeasurable within the resolution of our TR-SAXS experiments. In all cases, increasing the strain amplitude at a given frequency decreases the observed intensities of any intermediate σ phase reflections remaining after 20 min. These results illustrate that shear processing can be used to control the rates of order-order phase transformations in self-assembled soft materials that are otherwise slow under quiescent thermal annealing conditions. The shearmodulated control of these various transformations likely stems from complex changes in the frequencies of interparticle collisions, micelle rearrangements with minimal coronal overlap, intermicellar chain exchange, and activation of slip systems within the polycrystalline domains of the material.

These findings illustrate the potential for shear processing to control the rates of phase transitions in self-assembled structures in soft matter, which will inform the formulation and processing of aqueous dispersions of oligomeric and polymeric surfactants at high solids contents.

ASSOCIATED CONTENT

Supporting Information

The Supporting Information is available free of charge at https://pubs.acs.org/doi/10.1021/acsmacrolett.1c00154.

Experimental details, thermal annealing methods, sample preparation, additional SAXS data, and time scale extraction (PDF)

AUTHOR INFORMATION

Corresponding Authors

Lynn M. Walker — Department of Chemical Engineering, Carnegie Mellon University, Pittsburgh, Pennsylvania 15213, United States; © orcid.org/0000-0002-7478-9759; Email: lwalker@andrew.cmu.edu

Mahesh K. Mahanthappa – Department of Chemical Engineering and Materials Science, University of Minnesota, Minneapolis, Minnesota 55455, United States; oocid.org/ 0000-0002-9871-804X; Email: maheshkm@umn.edu

Authors

Connor S. Valentine — Department of Chemical Engineering, Carnegie Mellon University, Pittsburgh, Pennsylvania 15213, United States; © orcid.org/0000-0002-7783-4017

Ashish Jayaraman — Department of Chemical Engineering and Materials Science, University of Minnesota, Minneapolis, Minnesota 55455, United States; ⊙ orcid.org/0000-0001-7071-7419

Complete contact information is available at: https://pubs.acs.org/10.1021/acsmacrolett.1c00154

Notes

The authors declare no competing financial interest.

ACKNOWLEDGMENTS

M.K.M. and A.J. gratefully acknowledge funding from the National Science Foundation (CHE-1807330). C.S.V. and L.M.W. gratefully acknowledge a fellowship from PPG Industries, Inc., and the Dowd Fellows Program at CMU. Preliminary SAXS analyses were performed at the Characterization Facility at the University of Minnesota, which receives partial support from NSF through the MRSEC program (DMR-2011401). Synchrotron SAXS experiments were performed at the 12-ID-B beamline of the Advanced Photon Source, a U.S. Department of Energy (DOE) Office of Science User Facility operated by Argonne National Laboratory under Contract DE-AC02-06CH11357.

■ REFERENCES

- (1) Mezzenga, R.; Seddon, J. M.; Drummond, C. J.; Boyd, B. J.; Schröder-Turk, G. E.; Sagalowicz, L. Nature-Inspired Design and Application of Lipidic Lyotropic Liquid Crystals. *Adv. Mater.* **2019**, 31, 1900818.
- (2) Hyde, S. T. Identification of Lyotropic Liquid Crystalline Mesophases. In *Handbook of Applied Surface and Colloid Chemistry*; Holmberg, K., Shah, D. O., Schwuger, M. J., Eds.; John Wiley & Sons, Ltd.: West Sussex, 2002; Vol. 3, pp 299–327.

- (3) Lodge, T. P.; Pudil, B.; Hanley, K. J. The Full Phase Behavior for Block Copolymers in Solvents of Varying Selectivity. *Macromolecules* **2002**, *35*, 4707–4717.
- (4) Shearman, G. C.; Tyler, A. I. I.; Brooks, N. J.; Templer, R. H.; Ces, O.; Law, R. V.; Seddon, J. M. Ordered Micellar and Inverse Micellar Lyotropic Phases. *Liq. Cryst.* **2010**, *37*, *679*–*694*.
- (5) McConnell, G. A.; Gast, A. P.; Huang, J. S.; Smith, S. D. Disorder-Order Transitions in Soft Sphere Polymer Micelles. *Phys. Rev. Lett.* **1993**, *71*, 2102–2105.
- (6) Hamley, I. W.; Pople, J. A.; Diat, O. A Thermally Induced Transition from a Body-Centred to a Face-Centred Cubic Lattice in a Diblock Copolymer Gel. *Colloid Polym. Sci.* 1998, 276, 446–450.
- (7) Lodge, T. P.; Bang, J.; Park, M. J.; Char, K. Origin of the Thermoreversible Fcc-Bcc Transition in Block Copolymer Solutions. *Phys. Rev. Lett.* **2004**, 92, 145501.
- (8) Sakya, P.; Seddon, J. M.; Templer, R. H.; Mirkin, R. J.; Tiddy, G. J. T. Micellar Cubic Phases and Their Structural Relationships: The Nonionic Surfactant System C12EO12/Water. *Langmuir* **1997**, *13*, 3706–3714.
- (9) Kim, S. A.; Jeong, K.-J.; Yethiraj, A.; Mahanthappa, M. K. Low-Symmetry Sphere Packings of Simple Surfactant Micelles Induced by Ionic Sphericity. *Proc. Natl. Acad. Sci. U. S. A.* **2017**, *114*, 4072–4077.
- (10) Jayaraman, A.; Mahanthappa, M. K. Counterion-Dependent Access to Low-Symmetry Lyotropic Sphere Packings of Ionic Surfactant Micelles. *Langmuir* **2018**, *34*, 2290–2301.
- (11) Perroni, D. V.; Mahanthappa, M. K. Inverse Pm3n Cubic Micellar Lyotropic Phases from Zwitterionic Triazolium Gemini Surfactants. *Soft Matter* **2013**, *9*, 7919–7922.
- (12) Baez-Cotto, C. M.; Mahanthappa, M. K. Micellar Mimicry of Intermetallic C14 and C15 Laves Phases by Aqueous Lyotropic Self-Assembly Article. *ACS Nano* **2018**, *12*, 3226–3234.
- (13) Ungar, G.; Liu, Y.; Zeng, X.; Percec, V.; Cho, W. D. Giant Supramolecular Liquid Crystal Lattice. *Science* **2003**, 299, 1208–1211.
- (14) Yue, K.; Huang, M.; Marson, R. L.; He, J.; Huang, J.; Zhou, Z.; Wang, J.; Liu, C.; Yan, X.; Wu, K.; Guo, Z.; Liu, H.; Zhang, W.; Ni, P.; Wesdemiotis, C.; Zhang, W.-B.; Glotzer, S. C.; Cheng, S. Z. D. Geometry Induced Sequence of Nanoscale Frank-Kasper and Quasicrystal Mesophases in Giant Surfactants. *Proc. Natl. Acad. Sci. U. S. A.* 2016, 113, 14195–14200.
- (15) Lachmayr, K. K.; Wentz, C. M.; Sita, L. R. An Exceptionally Stable and Scalable Sugar-Polyolefin Frank-Kasper A15 Phase. *Angew. Chem., Int. Ed.* **2020**, *59*, 1521–1526.
- (16) Lindsay, A. P.; Lewis, R. M.; Lee, B.; Peterson, A. J.; Lodge, T. P.; Bates, F. S. A15, σ , and a Quasicrystal: Access to Complex Particle Packings via Bidisperse Diblock Copolymer Blends. *ACS Macro Lett.* **2020**, *9*, 197–203.
- (17) Mueller, A. J.; Lindsay, A. P.; Jayaraman, A.; Lodge, T. P.; Mahanthappa, M. K.; Bates, F. S. Emergence of a C15 Laves Phase in Diblock Polymer/Homopolymer Blends. *ACS Macro Lett.* **2020**, *9*, 576–582.
- (18) Lee, S.; Bluemle, M. J.; Bates, F. S. Discovery of a Frank-Kasper σ Phase in Sphere-Forming Block Copolymer Melts. *Science* **2010**, 330, 349–353.
- (19) Kim, K.; Schulze, M. W.; Arora, A.; Lewis, R. M., III; Hillmyer, M. A.; Dorfman, K. D.; Bates, F. S. Thermal Processing of Diblock Copolymer Melts Mimics Metallurgy. *Science* **2017**, *356*, 520–523.
- (20) Bates, M. W.; Lequieu, J.; Barbon, S. M.; Lewis, R. M.; Delaney, K. T.; Anastasaki, A.; Hawker, C. J.; Fredrickson, G. H.; Bates, C. M. Stability of the A15 Phase in Diblock Copolymer Melts. *Proc. Natl. Acad. Sci. U. S. A.* **2019**, *116*, 13194–13199.
- (21) Lee, S.; Leighton, C.; Bates, F. S. Sphericity and Symmetry Breaking in the Formation of Frank-Kasper Phases from One Component Materials. *Proc. Natl. Acad. Sci. U. S. A.* **2014**, *111*, 17723–17731.
- (22) Rappolt, M.; Cacho-Nerin, F.; Morello, C.; Yaghmur, A. How the Chain Configuration Governs the Packing of Inverted Micelles in the Cubic Fd3m-Phase. *Soft Matter* **2013**, *9*, 6291–6300.

- (23) Jayaraman, A.; Zhang, D. Y.; Dewing, B. L.; Mahanthappa, M. K. Path-Dependent Preparation of Complex Micelle Packings of a Hydrated Diblock Oligomer. *ACS Cent. Sci.* **2019**, *5*, 619–628.
- (24) Park, M. J.; Bang, J.; Harada, T.; Char, K.; Lodge, T. P. Epitaxial Transitions among FCC, HCP, BCC, and Cylinder Phases in a Block Copolymer Solution. *Macromolecules* **2004**, *37*, 9064–9075.
- (25) McConnell, G. A.; Lin, M. Y.; Gast, A. P. Long Range Order in Polymeric Micelles under Steady Shear. *Macromolecules* **1995**, 28, 6754–6764.
- (26) Lee, H. H.; Jeong, W.-Y.; Kim, J. K.; Ihn, K. J.; Kornfield, J. A.; Wang, Z.-G.; Qi, S. Orientational Proliferation and Successive Twinning from Thermoreversible Hexagonal-Body-Centered Cubic Transitions. *Macromolecules* **2002**, *35*, 785–794.
- (27) Wang, S.; Xie, R.; Vajjala Kesava, S.; Gomez, E. D.; Cochran, E. W.; Robertson, M. L. Close-Packed Spherical Morphology in an ABA Triblock Copolymer Aligned with Large-Amplitude Oscillatory Shear. *Macromolecules* **2016**, *49*, 4875–4888.
- (28) López-Barrón, C. R.; Wagner, N. J.; Porcar, L. Layering, Melting, and Recrystallization of a Close-Packed Micellar Crystal under Steady and Large-Amplitude Oscillatory Shear Flows. *J. Rheol.* **2015**, *59*, 793–820.
- (29) Hamley, I. Block Copolymers in Solution: Fundamentals and Applications. In *Concentrated Solutions: Flow Alignment*; Wiley: Chichester, England, 2012; Chapter 3.9, pp 149–158.
- (30) Koppi, K. A.; Tirrell, M.; Bates, F. S.; Almdal, K.; Colby, R. H. Lamellae Orientation in Dynamically Sheared Diblock Copolymer Melts. *J. Phys. II* **1992**, 2, 1941–1959.
- (31) Schulz, M. F.; Bates, F. S.; Almdal, K.; Mortensen, K. Epitaxial Relationship for Hexagonal-to-Cubic Phase Transition in a Block Copolymer Mixture. *Phys. Rev. Lett.* **1994**, *73*, 86–89.
- (32) Koppi, K. A.; Tirrell, M.; Bates, F. S.; Almdal, K.; Mortensen, K. Epitaxial Growth and Shearing of the Body Centered Cubic Phase in Diblock Copolymer Melts. *J. Rheol.* **1994**, *38*, 999–1027.
- (33) Pozzo, D. C.; Walker, L. M. Shear Orientation of Nanoparticle Arrays Templated in a Thermoreversible Block Copolymer Micellar Crystal. *Macromolecules* **2007**, *40*, 5801–5811.
- (34) Okamoto, S.; Saijo, K.; Hashimoto, T. Dynamic SAXS Studies of Sphere-Forming Block Copolymers under Large Oscillatory Shear Deformation. *Macromolecules* **1994**, *27*, 3753–3758.
- (35) Bang, J.; Lodge, T. P.; Wang, X.; Brinker, K. L.; Burghardt, W. R. Thermoreversible, Epitaxial Fcc < -> Bcc Transitions in Block Copolymer Solutions. *Phys. Rev. Lett.* **2002**, *89*, 215505.
- (36) Zana, R. Dynamics of Surfactant Self-Assembleys: Micelles, Microemulsions, Vesicles and Lyotropic Phases, 1st ed.; Zana, R., Ed.; CRC Press: Boca Raton, FL, 2005.
- (37) Phoon, C. L.; Higgins, J. S.; Allegra, G.; Van Leeuwen, P.; Staples, E. Shear Induced Crystallization and Melting of a Micellar Solution. *Proc. R. Soc. London, Ser. A: Math. Phys. Sci.* **1993**, 442, 221–230.
- (38) Fischer, S.; Exner, A.; Zielske, K.; Perlich, J.; Deloudi, S.; Steurer, W.; Lindner, P.; Förster, S. Colloidal Quasicrystals with 12-Fold and 18-Fold Diffraction Symmetry. *Proc. Natl. Acad. Sci. U. S. A.* **2011**, *108*, 1810–1814.
- (39) Valentine, C. S.; Walker, L. M. Rheological Characterization of BCC and FCC Structures in Aqueous Diblock Copolymer Liquid Crystals. *Korea Aust. Rheol. J.* **2019**, *31*, 249–254.
- (40) DeGraef, M.; McHenry, M. Structure of Materials: An Introduction to Crystallography, Diffraction, and Symmetry, 2nd ed.; Cambridge University Press: Cambridge, 2012.
- (41) Liu, Y.; Nie, H.; Bansil, R.; Steinhart, M.; Bang, J.; Lodge, T. P. Kinetics of Disorder-to-Fcc Phase Transition via an Intermediate Bcc State. *Phys. Rev. E: Stat. Nonlinear, Soft Matter Phys.* **2006**, *73*, 1–6.
- (42) Avrami, M. Kinetics of Phase Change. I General Theory. J. Chem. Phys. 1939, 7, 1103–1112.
- (43) Avrami, M. Kinetics of Phase Change. II Transformation-Time Relations for Random Distribution of Nuclei. *J. Chem. Phys.* **1940**, *8*, 212–224.
- (44) Avrami, M. Granulation, Phase Change, and Microstructure Kinetics of Phase Change. III. J. Chem. Phys. 1941, 9, 177–184.

- (45) Kim, K.; Arora, A.; Lewis, R. M.; Liu, M.; Li, W.; Shi, A.-C.; Dorfman, K. D.; Bates, F. S. Origins of Low-Symmetry Phases in Asymmetric Diblock Copolymer Melts. *Proc. Natl. Acad. Sci. U. S. A.* **2018**, *115*, 847–854.
- (46) Ziherl, P.; Kamien, R. D. Soap Froths and Crystal Structures. *Phys. Rev. Lett.* **2000**, *85*, 3528–3531.
- (47) Reddy, A.; Buckley, M. B.; Arora, A.; Bates, F. S.; Dorfman, K. D.; Grason, G. M. Stable Frank-Kasper Phases of Self-Assembled, Soft Matter Spheres. *Proc. Natl. Acad. Sci. U. S. A.* **2018**, *115*, 10233–10238.
- (48) Callister, W. D.; Rethwisch, D. G. Materials Science and Engineering: An Introduction, 8th ed.; John Wiley & Sons: New York, 2011.
- (49) Wright, R. N.; Bok, K. A. A15 Compound Deformation and Secondary Slip in V3Si. *Metall. Trans. A* 1988, 19, 1125–1127.